Highly Anisotropic Mechanical Response of the Van der Waals Magnet CrPS$_4$

Maurits J. A. Houmes, Samuel Mañas-Valero,* Alvaro Bermejillo-Seco, Eugenio Coronado, Peter G. Steeneken, and Herre S. J. van der Zant*

Semiconducting van der Waals magnets exhibit a rich physical phenomenology with different collective excitations, as magnons or excitons, that can be coupled, thereby offering new opportunities for optoelectronic, spintronic, and magnonic devices. In contrast with the well-studied van der Waals magnets CrI$_3$ or Fe$_3$GeTe$_2$, CrPS$_4$ is a layered metamagnet with a high optical and magnon transport anisotropy. Here, the structural anisotropy of CrPS$_4$ above and below the magnetic phase transition is investigated by fabricating nanomechanical resonators. A large anisotropy is observed in the resonance frequency of resonators oriented along the crystalline a- and b-axis, indicative of a lattice expansion along the b-axis, boosted at the magnetic phase transition, and a rather small continuous contraction along the a-axis. This behavior in the mechanical response differs from that previously reported in van der Waals magnets, as FePS$_3$ or CoPS$_3$, and can be understood from the quasi-1D nature of CrPS$_4$. The results pinpoint CrPS$_4$ as a promising material in the field of low-dimensional magnetism and show the potential of mechanical resonators for unraveling the in-plane structural anisotropy coupled to the magnetic ordering that, in a broader context, can be extended to studying structural modifications in other 2D materials and van der Waals heterostructures.

1. Introduction

Anisotropy is a fundamental property necessary to fully understand the behavior of low-dimensional materials.[1] For instance,

M. J. A. Houmes, S. Mañas-Valero, A. Bermejillo-Seco, P. G. Steeneken, H. S. J. van der Zant
Kavli Institute of Nanoscience
Delft University of Technology
Lorentzweg 1, Delft 2628 CJ, The Netherlands
E-mail: S.ManasValero@tudelft.nl; h.s.j.vanderzant@tudelft.nl

E. Coronado
Instituto de Ciencia Molecular (ICMol)
Universitat de València
c/Catedrático José Beltrán 2, 46980 Paterna, Spain

long-range magnetic order was long thought to be forbidden in the 2D limit, as per the Mermin-Wagner theorem,[2] but this theorem can be circumvented if magnetic anisotropy is present, as this allows for the stabilization of different magnetic configurations.[3] Anisotropic behaviors are not limited to magnetic systems as they can also be observed in, for example, the electronic, optical, and structural properties. In fact, these anisotropic properties are often coupled, offering a fruitful avenue for the control of collective excitations, such as excitons, phonons, or magnons, and allowing the design of new devices in fields such as magnonics, spintronics, optoelectronics, or information storage and processing.[4,5] In this regard, van der Waals magnets with in-plane anisotropy offer unique opportunities, both in the fundamental understanding of these materials and in terms of applications, as recently shown by the exciton-magnon coupling reported for CrSBr or the fabrication of spintronic and magnonic devices based on 2D magnets,[6–10] among others.

A promising van der Waals magnet exhibiting an interplay between the optical, electrical, magnetic, and structural properties is the magnetic van der Waals semiconductor CrPS$_4$.[11–14] A single layer of CrPS$_4$ consists of edge-sharing CrS$_6$ octahedra forming quasi-1D chains along the b-axis that are interconnected along the a-axis by PS$_4$ tetrahedra, **Figure 1**a, thus exhibiting a marked low-dimensional character.[14,15] Magnetically, CrPS$_4$ is an A-type antiferromagnet, where ferromagnetic layers are coupled antiferromagnetically along the c-axis, Figure 1b, below ca. 34 K, as corroborated by magnetic susceptibility measurements, Figure 1c, and in agreement with previous results in literature, where a rich magnetic phase diagram, including spin-flop and spin-flip transitions, is reported.[11,16,17] Optically, it exhibits a marked anisotropic behavior, as determined by Raman spectroscopy or photoluminescence measurements; excitonic emission is furthermore tuneable by temperature and thickness.[12–14,18] CrPS$_4$ can be thinned down to the single layer limit while preserving its magnetic ordering,[19] and thin-layers have been incorporated into electronic devices, showing magnetic states controllable by the gate voltage.[20] In addition, the insulating nature of CrPS$_4$ at low temperatures is ideal for the electrical excitation and detection of magnons,[6] and the

ADVANCED
SCIENCE NEWS
www.advancedsciencenews.com

ADVANCED
FUNCTIONAL
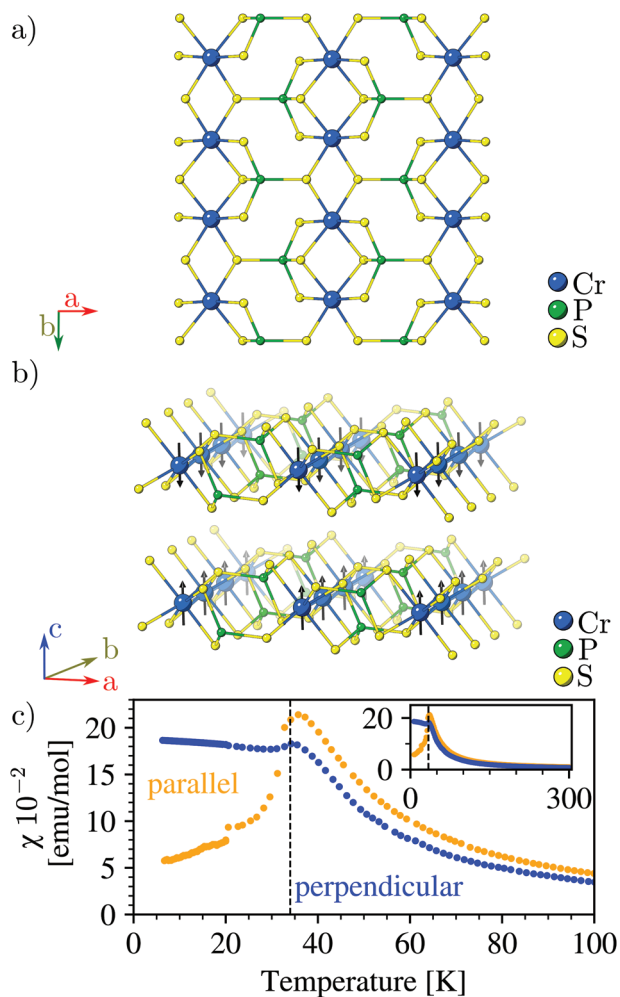**MATERIALS**
www.afm-journal.de

Figure 1. a) CrPS$_4$ crystal structure along the ab-plane, in which CrS$_6$ octahedra form quasi-1D chains (up-down) connected via PS$_4$ tetrahedra. The crystallographic a- and b-axis are indicated using red and green arrows, respectively. The Cr, P, and S atoms are colored blue, green, and yellow respectively. b) Layered structure of CrPS$_4$; same color coding as in a). The magnetic spin structure in the antiferromagnetic phase is indicated by the black arrows through the Cr atoms. They are ferromagnetically aligned in-plane and antiferromagnetically between the planes. c) Temperature dependence of the magnetic susceptibility under 1 kOe field applied parallel (orange), and perpendicular (blue) to the c-axis. The transition temperature is indicated with a black dashed line. The parallel and perpendicular susceptibility show different behavior below the transition. The inset shows the extended temperature range (6 − 300 K) of the same data.

fabrication of multi-bit read-only memories.[21] Despite the exciting properties of CrPS$_4$ described above, the role of the underlying in-plane anisotropic structural behavior remains still unexplored.

Here, we take advantage, on the one hand, of the van der Waals nature of CrPS$_4$ for fabricating nanomechanical resonators based on the layered structure of the material and, on the other hand, of the high sensitivity of nanomechanical resonators to the strain concomitant to a structural modification.[22–26] We observe a large in-plane structural anisotropy while cooling down, exhibiting a striking opposite mechanical behavior along the a- and b-axes. We

also find indications of a previously unreported structural transition above 120 K.

2. Results and Discussion

Crystals of CrPS$_4$ are grown by chemical vapor transport (see Experimental section). Thin layers of CrPS$_4$ are mechanically exfoliated from their bulk counterpart and deterministically transferred on top of cavities etched in a SiO$_2$ on Si substrate, thereby forming a nanomechanical resonator. Typical flake thicknesses suitable for covering homogeneously the cavities are in the range of 40 – 120 nm. Developing chemical routes for reaching atomically thin layers of CrPS$_4$ with larger lateral sizes may enable to study the mechanical properties of CrPS$_4$ down to the 2D limit. The fundamental mechanical resonance is characterized as a function of the temperature using a laser interferometry technique **Figure 2**a; see Experimental Section). In particular, our experimental configuration is based on an optical interferometer where the CrPS$_4$ membrane acts as the moving mirror, and the silicon surface at the bottom of the drum as the fixed mirror. Thus, by focusing a red laser (Helium-Neon laser, $\lambda = 632.8$ nm) on the CrPS$_4$ membrane, we can track its motion since the amplitude of the vibration modifies the cavity length and, therefore, constructive or destructive interference takes place. The interference changes the intensity of the reflected light from the cavity, which is detected with a photodiode. Another mechanism that plays a role is the modulated absorption of the light by the CrPS$_4$ drum.[27] The motion of the membrane is triggered photothermally by focusing a blue diode laser on it ($\lambda = 405$ nm). The resonance frequency depends on the geometry, the material properties (Young's modulus, density, and Poisson's ratio) as well as the strain. Therefore, variations in the temperature imply a contraction or expansion of the unit cell of the material that causes tensile or compressive strain and, consequently, modifies the resonance frequency. Thus, an enhancement (decrease) of the resonance frequency relates to a compression (expansion) of the unit cell.[25]

2.1. Circular Cavity

A typical resonance response of a circular resonator is shown in Figure 2b. This response is fitted using a Lorentzian function as shown by the orange curve in Figure 2b. From this fit the resonance frequency, f_0, is extracted. Since the resonance frequency is the lowest in the spectrum, we attribute it to the fundamental mode. The dependence of the fundamental resonance frequency on temperature is shown in Figure 2c.

A clear change in the resonance frequency over the measured temperature range is present: in the region between 60 and 40 K the frequency slowly decreases with decreasing temperature, whereas in the region below 40 K this decrease becomes stronger until around 28 K where the decrease becomes, weaker appearing to level out at 10 K. No significant thermal hysteresis between the heating and cooling cycles is observed (compare the blue and red dots). A decrease in the resonance frequency, also called softening, implies a decrease in tensile strain in the material. Since, in this case, the decrease occurs solely as a response
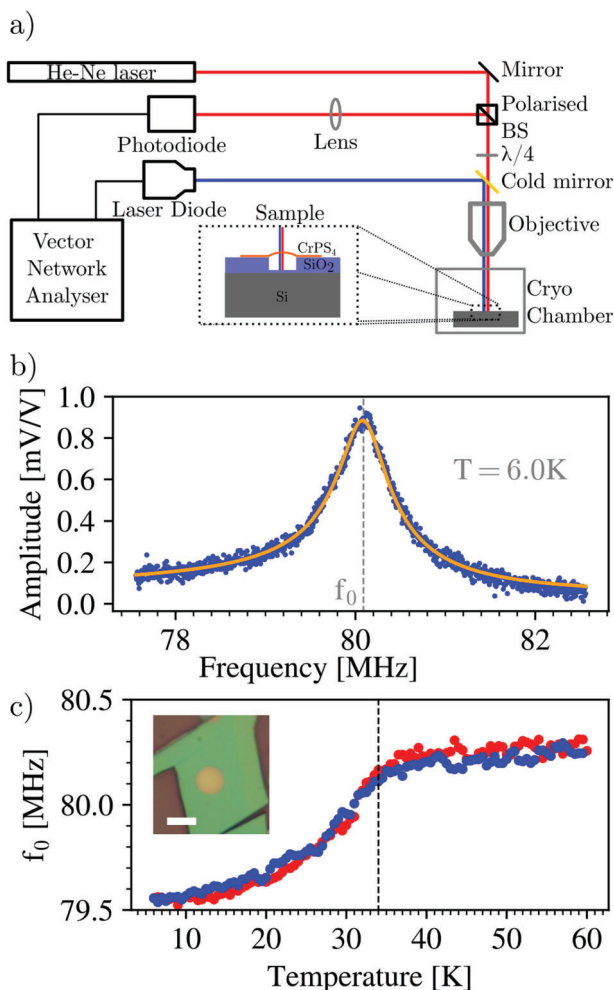
**ADVANCED
SCIENCE NEWS**

www.advancedsciencenews.com

**ADVANCED
FUNCTIONAL
MATERIALS**

www.afm-journal.de

a)

b)

c)

Figure 2. a) Schematics of the measurement setup. The vector network analyser (VNA) power modulates a laser diode ($\lambda = 405$ nm), as to actuate the vibrations of the drum in the cryo-chamber. Motion is read out with a photodiode connected to the VNA using a He-Ne laser ($\lambda = 632$ nm), a polarized beam-splitter (BS), and a quarter-wave plate ($\lambda/4$) to create an interferometer. Note, that the red and blue laser paths are offset for clarity but in reality they are co-incident. The zoom-in of the sample shows a schematic cut-through. b) Representative frequency response, measured at 6 K. The blue dots are the experimental data and the orange line is a harmonic oscillator fit to them, defining the resonance frequency (gray dashed line), indicated by f_0. c) Resonance frequency as a function of temperature between 6 and 60 K. There is no significant difference between the heating (red) and cooling (blue) cycles. The inset shows an optical microscope image of a circular drum sample. The scale bar is 4 μm. Data shown in panels (b) and (c) correspond to a 120 nm thick $CrPS_4$ flake.

to a change in temperature, this softening implies an expansion of the crystal lattice when cooling down, indicative of a negative thermal expansion coefficient (TEC). This is comparable to previous results on the 2D magnet $Cr_2Ge_2Te_6$,[22] also displaying an softening response. Here softening is somewhat unexpected as the related compounds of transition metal thiophosphates (such as $FePS_3$, $MnPS_3$, $CoPS_3$, or $NiPS_3$),[23,25] show an increase of f_0 with decreasing temperature (hardening); previously reported measurements on the same material, $CrPS_4$, by Li et al.,[28] also show a hardening response, in contrast to our results.

2.2. Rectangular Cavities

A possible reason for the difference with the previously reported measurements is the fact that those measurements were done on a beam geometry for which alignment of the crystal is relevant, especially for anisotropic materials such as $CrPS_4$. Therefore ,we further investigate the anisotropic contributions to this strain behavior. In order to isolate the contributions of different crystallographic axes, we create star samples, which consist of an array of rectangular cavities arranged radially with a rotational offset of 30 degrees. By transferring a flake of $CrPS_4$ over the entire star multiple rectangular drums are created each with a different orientation with respect to the crystallographic axes.[23] By combining two star patterns with an offset with respect to each other of 15 degrees, the angular resolution is increased, albeit requiring larger flakes of the material. An optical image of such a sample is given in **Figure 3**a. The crystallographic a- and b-axes are determined as reported by Lee et al.;[14] they are indicated by the red and green arrows, respectively.

We then compare the resonance frequencies of the cavities with their short axis along the a- and b-axis respectively, see Figure 3b. Strikingly different behavior is observed between the two directions. For the b-axis, a softening of the mode occurs while cooling, similar to the observation for circular drums, indicative of decreasing tensile and a negative TEC. In contrast, the resonance frequency of the a-axis orientation shows a small increase in the resonance frequency over the same temperature range. This increase indicates increasing tensile strain while lowering the temperature; there is no significant feature present near the phase transition point in this case.

This behavior can be understood as a result of an expansion between the Cr centers along the quasi-1D chains (b-axis), which is enhanced upon the magnetic phase transition, and a rather steady and small compression for the orthogonal direction, that does not exhibit a discontinuity at the phase transition. These findings are in line with the reported crystal structure above and below the magnetic transition, where an expansion of the b-axis is observed while cooling from 60 to 4 K.[17] For completeness, the temperature dependence for different angular directions is presented in Figure 3c, which emphasizes the clear anisotropic dependence of the resonance frequency and thus the lattice constants of the material. Similar trends are observed for other circular and star drums (see Sections S1 and S2, Supporting Infromation), manifesting the robustness of the underlying physical phenomena. Overall, we observe a pronounced negative thermal expansion along the b-axis and a small positive thermal expansion along the a-axis. The presence of such a uniaxial negative TEC is a typical fingerprint of highly anisotropic systems, as occurring in related compounds including metal halides, oxychlorides, or CrSBr.[4,29–31] This difference in the thermal expansion coefficients along the a- and b-axes that appears below 120 K and persists down to low temperature may arise from differences in the Grüneisen parameter along the different crystal axes, which leads to an increasing anisotropy that eventually can contribute to the magnetic phase transition at lower temperature. These results may motivate further research on the $CrPS_4$ properties at temperatures well above the magnetic transition.
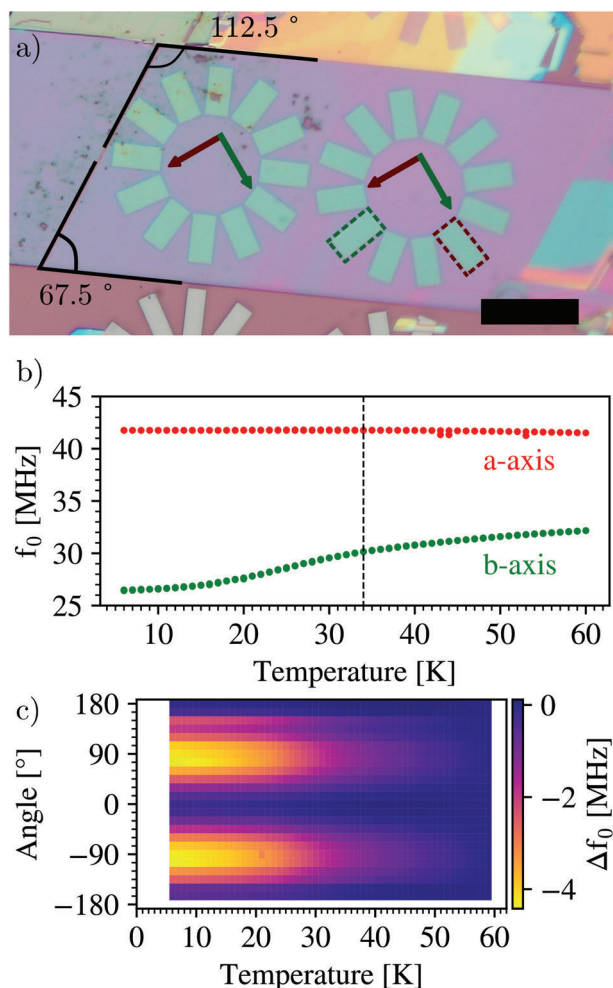
ADVANCED
SCIENCE NEWS

www.advancedsciencenews.com

ADVANCED
FUNCTIONAL
MATERIALS

www.afm-journal.de

Figure 3. a) Optical microscopy picture of a star sample, displaying two arrays of rectangular cavities covered by a flake of CrPS$_4$. In the lower left corner of the flake, the fracture angle is highlighted and measured to be 67.5°. From this and the opposite angle of 112.5° the crystallographic axes are determined. The crystallographic a- (red) and b-axis (green) are indicated by colored arrows. The cavity highlighted red and green corresponds to the cavity with its short axis aligned along the a- (0°) and b-axis (90°), respectively. The scale bar is 20 μm. b) Resonance frequency as a function of temperature between 6 and 60 K for two cavities of the same flake with their short axes aligned along the crystallographic a-axis (red) and b-axis (green). There is a clear difference between the two directions, with the a-axis showing no significant change in resonance frequency, and the b-axis showing a transition behavior similar to that seen in circular drums (Figure 2) when crossing the phase transition (black dashed line). c) Relative frequency change (color coded) with respect to 60 K as a function of temperature. The angle corresponds to the angle that the short axis of the cavity makes with the crystallographic a-axis; the cavity with the short axis parallel to the crystallographic a-axis corresponds to 0°. Data shown in panels (b) and (c) correspond to a 75 nm thick CrPS$_4$ flake.

2.3. Phase Transition

Above about 120 K, **Figure 4**a shows that the frequencies along the a- and b-axis exhibit the same temperature dependence. This indicates an equal expansion of the lattice for both axes as temperature decreases. However, around 120 K, the distance between

the green and red curves starts to become larger, indicating a smaller expansion rate for the b-axis. Indeed, at $T \simeq 80$ K we observe an upturn in the slope for the b-axis in the resonance frequency versus temperature dependence, shifting from a positive slope at low temperatures - expansion of the b-axis while cooling down from 80 to 6 K, in line with the neutron experiments in bulk CrPS$_4$ reported by Calder et al.[17] or Peng et al.[32] - to a negative one - compression of the b-axis while cooling from room
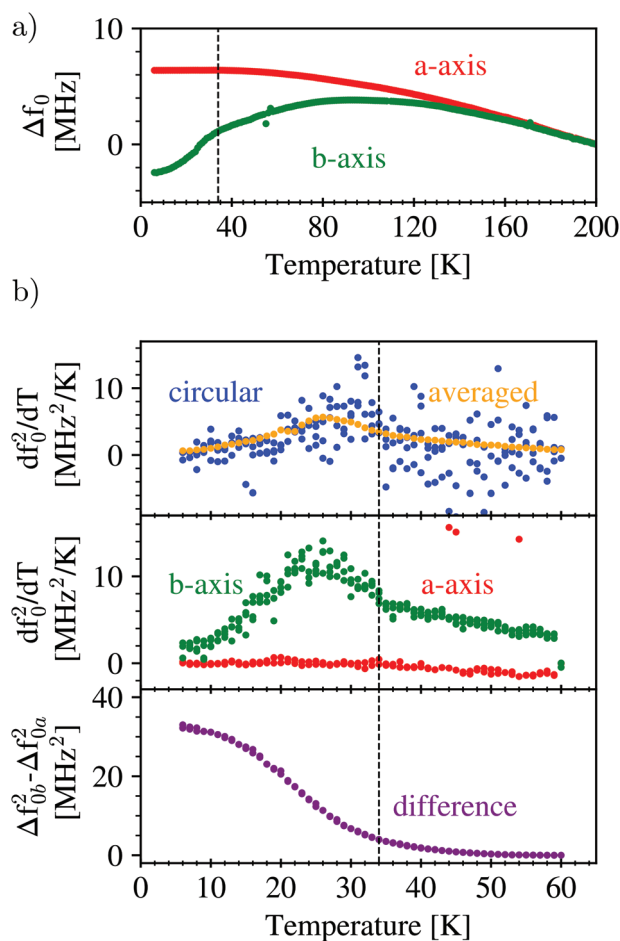

Figure 4. a) Relative change in resonance frequency w.r.t. its value at 200 K as a function of temperature between 6 and 200 K for two cavities of the same flake with their short axis aligned along the crystallographic a-axis (red) and b-axis (green). The data is the extended version from the data shown in Figure 3b and serves to highlight that for temperatures above 120 K the two axes have the same behavior. b) Top panel: derivative of the frequency squared with respect to temperature as a function of temperature of a circular cavity (blue) and averaged over all rectangular cavities in a star sample (orange). The average shows a peak around 25 K, whereas the circular cavity has a peak closer to 30 K. Middle panel: derivative of the frequency squared with respect to temperature as a function of temperature for two rectangular cavities with their short axis aligned along the a- (red) and b-axis (green), respectively. The a-axis shows no clear variation with temperature whereas the b-axis shows a peak around 25 K. Bottom panel: difference between the change in frequency squared for two rectangular cavities with their short axis aligned along the b- and a-axis, respectively. The bulk transition temperature is indicated with the vertical black dashed line. Data shown in panels (a) and (b, c) correspond to a 120 nm and 75 nm thick CrPS$_4$ flake, respectively.

**ADVANCED
SCIENCE NEWS**

www.advancedsciencenews.com

**ADVANCED
FUNCTIONAL
MATERIALS**

www.afm-journal.de

temperature down to 80 K. This structural anisotropy enhancement around 120 K is to our knowledge unreported in literature. This increased anisotropy and expansion of the quasi-1D chains along the b-axis upon cooldown illustrates the interplay between lattice parameters and magnetic order that, based on the change in slope of the $f_0(T)$ curve, indicates that magnetic ordering also has a substantial influence on the lattice parameters, leading to further chain expansion.

Near the phase transition, the change in frequency for the green curve (b-axis) is even more pronounced. In contrast, the red curve (a-xis) shows a flattening off as temperature decreases with no clear features. To further characterize the behavior near the transition, we investigate the temperature derivative of the frequency squared, $\frac{df_0^2}{dT}$, as it is shown that this quantity is proportional to the specific heat.[25] It is expected to have an anomaly at the phase transition. Plotting the $\frac{df_0^2}{dT}$ as a function of temperature, Figure 4b, we find that in the case of a circular drum this $\frac{df_0^2}{dT}$ exhibits a peak around 30 K, below the expected transition temperature of 34 K. An even lower peak at 25 K is found for the average behavior of a star sample, which is calculated by adding up the response of all cavities with different angles and dividing the total by the number of cavities involved.

The reason for the discrepancy between the peak in $\frac{df_0^2}{dT}$ and the expected transition temperature is unclear but can have several origins. It can be that the transition temperature is shifted from the bulk value simply by going to thinner samples of the material as it transitions to the value of a monolayer, although the samples in this study are still quite thick, ranging from 40 to 165 nm, for this to be such a large effect. Another reason for the deviation from bulk value can be that the strain in these samples shifts the transition temperature.[22,25] Since we do not apply any external strain, the strain responsible for this shift at the transition temperature should be entirely due to the thermal expansion induced strain accumulated upon cool down of the samples. However, the change in strain required to account for the observed shift is much larger than can be rationalized by the temperature induced strain. A third reason can be that there is an additional contribution in the $\frac{df_0^2}{dT}$, which dominates the peak caused by the anomaly in the specific heat. Below the transition, magnetostriction, which couples the magnetic order parameter to strain can give such a contribution, which we will now consider in more detail. Strain or pressure modifies the bond distances - that is, the superexchange pathways - and, within the Goodenough-Kanamori-Arderson superexchange mechanism, the magnetic exchange. Indeed, Bud'ko et al.[16] have reported a suppression of the Néel temperature of bulk CrPS$_4$ while applying hydrostatic pressure.

Assuming the magnetostrictive coupling coefficient to be temperature independent, we expect a peak in the $\frac{df_0^2}{dT}$, which coincides with the steepest slope in the order parameter. This is consistent with the slope of $\Delta f_{0b}^2 - \Delta f_{0a}^2$, Figure 4c, which is proportional to the order parameter squared, L^2, with the peak observed in $\frac{df_0^2}{dT}$.[23] So the curve in this figure gives an impression of the temperature dependence of the order parameter. The curve does not follow the standard shape from mean-field theory as the change at the transition temperature is not as abrupt. A possi-

ble explanation is that the anisotropy present is not due to the magnetic order, but further research is needed to verify this.

Comparing the $\frac{df_0^2}{dT}$ of the two different crystallographic axes a peak around 25 K is present for the b-axis while no such feature is present along the a-axis. The fact that no sign of the phase transition is visible in the a-axis can be understood from the fact that the coupling between $\frac{df_0^2}{dT}$ and the specific heat is dependent on the TEC. Since the TEC along the a-axis around the transition is very small, as can be seen from the fact that the frequency does not vary with temperature, this coupling along the a-axis is extremely weak.

Since $\frac{df_0^2}{dT}$ is proportional to the TEC of the material,[25] the data of Figure 4b can be used to estimate the TEC along the two crystalline directions. By using the approximate frequency for a rectangular drum of high aspect ratio:[23]

$$f_0 \approx \frac{1}{2} \sqrt{\frac{E}{\rho w^2}} \epsilon \tag{1}$$

we find an adjusted formula for the TEC in rectangular drums,

$$\alpha = -\frac{4\rho w^2}{E} \frac{df_0^2}{dT}(T) + \alpha_{\text{Si}}(T) \tag{2}$$

here, E is the Young's modulus, ρ the density, and w the length of the cavity along its short direction. CrPS$_4$ is expected to have an anisotropic Young's modulus,[33] with the values along the a-(E_a) and b-axis (E_b) being respectively $E_a = 99.23$ GPa and $E_b = 64.53$ GPa, (see Section S3, Supporting Information).[34] The values for the density, (ρ), and the width of the cavity, (w), are 2.9×10^3 Kg m^{-3},[35] and 4 µm, respectively. For $\alpha_{\text{Si}}(T)$ we use the data of Lyon et al.[36] This results in a TEC along the a- and b-axis of 2×10^{-8} and -4×10^{-5} K^{-1} at 26 K (see Section S3, Supporting Information).

3. Conclusion

In conclusion, we have probed by nanomechanical resonators a large structural anisotropy in thin layers of the van der Waals metamagnet CrPS$_4$. While cooling down, we observe a continuously increasing tensile strain along the a-axis, but a decreasing tensile strain along the b-axis, that is largely enhanced upon the magnetic phase transition. This suggests an increase in the distances between the Cr^{3+} ions along the quasi-1D chain direction. Our results highlight CrPS$_4$ as a van der Waals magnet that is relevant for low-dimensional magnetism due to its marked anisotropic behavior, in stark contrast with the most common structurally isotropic 2D magnets, such as CrI$_3$.[37] We also show that when using nanomechanical resonators for studying van der Waals magnets, careful choice of geometry is needed to account for anisotropic effects. This provides an important insight for future research directions, such as the anisotropic mechanical coupling in van der Waals heterostructures formed by distinct 2D materials or the role of collective excitations, like magnons or excitons, in the 2D limit.

4. Experimental Section

Crystal Growth: Crystals of $CrPS_4$ were grown following a solid-state reaction inside a sealed evacuated quartz tube (pressure 5×10^{-5} mbar, length: 50 cm, internal diameter: 14 mm) with a stoichiometric amount of Cr (99.99 %, Alfa-Aesar), P (>99.99 %, Sigma–Aldrich) and S (99.99 %, Sigma–Aldrich). A three-zone furnace was used, with the material placed in the leftmost zone, with a temperature gradient of 750/650/700 °C. The temperature was kept constant for 21 days and rapidly quenched into water. With this process crystals with a length of up to several centimetres were obtained. The obtained crystals were analyzed by energy-dispersive X-ray spectroscopy and by powder X-ray diffraction. The amount of elements obtained was Cr: 23.3 ± 0.5 %, P: 14.8 ± 0.4 % and S: 61.8 ± 1.5%, in good agreement with the expected ones (Cr: 24.6 %, P: 14.7 % and S: 60.7 %). The refinement of the X-ray pattern (ICSD 25059) revealed a monoclinic C face center crystal system with C121 space group and a unit cell determined by $\alpha = \gamma = 90°$ and $\beta = 91.99(1)°$ and a = 10.841(9) Å, b = 7.247(6) Å and c = 6.100(5) Å. The obtained results were in accordance with the ones reported in the literature.[11]

Bulk Magnetic Measurements: Variable-temperature $(2 - 300$ K) direct current (d.c.) magnetic susceptibility measurements were carried out in an applied field of 1.0 kOe with a SQUID magnetometer (Quantum Design MPMS-XL-5).

Sample Fabrication: Substrates consist of thermal SiO_2 of 285 nm thickness, grown on highly doped (Si^{++}) silicon. The rectangular cavities were defined via e-beam lithography using AR-P 6200 resist. After development, the exposed SiO_2 areas were fully etched via reactive ion etching. The AR-P 6200 resist was stripped in PRS-3000 and the sample was cleaned in an O_2 plasma before stamping. The exfoliation and transfer of multi-layer $CrPS_4$ flakes were done using a combination of polydimethylsiloxane (PDMS) and polycarbonate (PC) transfer methods. First, $CrPS_4$ crystals were exfoliated onto the PDMS through scotch tape. Selected flakes were then transferred to the star-shaped cavities in the SiO_2/Si substrate. For transfer of circular drum samples, the $CrPS_4$ crystals were exfoliated using scotch tape directly on un-etched Si/SiO_2 substrates. Selected flakes are then transferred to circular-shaped cavities in the SiO_2/Si substrate using PC on PDMS.[38]

Laser Interferometry: Samples were mounted on a heater stage, which was cooled down to 4 K using a Montana Instruments Cryostation s50 cryostat with optical access. A blue diode laser ($\lambda = 405$ nm) was used to excite the membrane optothermally via AC power modulation from a vector network analyzer (VNA). Displacements were detected by focusing a red He-Ne laser beam ($\lambda = 632$ nm) on the cavity formed by the membrane and Si substrate. The reflected light, which was modulated by the position-dependent membrane motion, was recorded by a photodiode and processed by a phase-sensitive VNA. Laser spot size was $\approx 1\,\mu$m.

Atomic Force Microscopy: Samples were mounted in a Cypher AFM platform from Asylum Research under atmospheric conditions and scanned using Bruker FASTSCAN-A tips. In order to minimize contamination of the samples AFM was performed after all other measurements.

Supporting Information

Supporting Information is available from the Wiley Online Library or from the author.

Acknowledgements

Conflict of Interest

The authors declare no conflict of interest.

Data Availability Statement

The data that support the findings of this study are available from the corresponding author upon reasonable request.

Keywords

[1] Z. da Gao, Z. hui yi Jiang, J. dong Li, B. wen Li, Y. yang Long, X. mei Li, J. Yin, W. lin Guo, *Adv. Eng. Mater.* **2022**, *24*, 2200519.

[2] N. D. Mermin, H. Wagner, *Phys. Rev. Lett.* **1966**, *17*, 1133.

[3] M. Gibertini, M. Koperski, A. F. Morpurgo, K. S. Novoselov, *Nat. Nanotechnol.* **2019**, *14*, 408.

[4] J. Wang, Q. Gao, Y. Gao, Y. Luo, J. Guo, Q. Sun, E. Liang, *Appl. Phys. Lett.* **2021**, *118*, 222105.

[5] G. M. Diederich, J. Cenker, Y. Ren, J. Fonseca, D. G. Chica, Y. J. Bae, X. Zhu, X. Roy, T. Cao, D. Xiao, X. Xu, *Nat. Nanotechnol.* **2022**, *18*, 23.

[6] D. K. de Wal, A. Iwens, T. Liu, P. Tang, G. E. W. Bauer, B. J. van Wees, *Phys. Rev. B* **2023**, *107*, L180403.

[7] K. Hwangbo, Q. Zhang, Q. Jiang, Y. Wang, J. Fonseca, C. Wang, G. M. Diederich, D. R. Gamelin, D. Xiao, J. H. Chu, W. Yao, X. Xu, *Nat. Nanotechnol.* **2021**, *16*, 655.

[8] S. Kang, K. Kim, B. H. Kim, J. Kim, K. I. Sim, J. U. Lee, S. Lee, K. Park, S. Yun, T. Kim, A. Nag, A. Walters, M. Garcia-Fernandez, J. Li, L. Chapon, K. J. Zhou, Y. W. Son, J. H. Kim, H. Cheong, J. G. Park, *Nature* **2020**, *583*, 785.

[9] C. Boix-Constant, S. Mañas-Valero, A. M. Ruiz, A. Rybakov, K. A. Konieczny, S. Pillet, J. J. Baldoví, E. Coronado, *Adv. Mater.* **2022**, *34*, 2204940.

[10] Y. J. Bae, J. Wang, A. Scheie, J. Xu, D. G. Chica, G. M. Diederich, J. Cenker, M. E. Ziebel, Y. Bai, H. Ren, C. R. Dean, M. Delor, X. Xu, X. Roy, A. D. Kent, X. Zhu, *Nature* **2022**, *609*, 282.

[11] Y. Peng, S. Ding, M. Cheng, Q. Hu, J. Yang, F. Wang, M. Xue, Z. Liu, Z. Lin, M. Avdeev, Y. Hou, W. Yang, Y. Zheng, J. Yang, *Adv. Mater.* **2020**, *32*, 2001200.

[12] M. Riesner, R. Fainblat, A. K. Budniak, Y. Amouyal, E. Lifshitz, G. Bacher, *J. Chem. Phys.* **2022**, *156*, 54707.

[13] P. Gu, Q. Tan, Y. Wan, Z. Li, Y. Peng, J. Lai, J. Ma, X. Yao, S. Yang, K. Yuan, D. Sun, B. Peng, J. Zhang, Y. Ye, *ACS Nano* **2020**, *14*, 1003.

[14] J. Lee, T. Y. Ko, J. H. Kim, H. Bark, B. Kang, S. G. Jung, T. Park, Z. Lee, S. Ryu, C. Lee, *ACS Nano* **2017**, *11*, 10935.

[15] R. Diehl, C.-D. Carpentier, *Acta Crystallogr.* **1978**, *B34*, 1097.

[16] S. L. Bud'Ko, E. Gati, T. J. Slade, P. C. Canfield, *Phys. Rev. B* **2021**, *103*, 224407.

[17] S. Calder, A. V. Haglund, Y. Liu, D. M. Pajerowski, H. B. Cao, T. J. Williams, V. O. Garlea, D. Mandrus, *Phys. Rev. B* **2020**, *102*, 024408.

ADVANCED
SCIENCE NEWS

www.advancedsciencenews.com

ADVANCED
FUNCTIONAL
MATERIALS

www.afm-journal.de

[18] S. Kim, S. Yoon, H. Ahn, G. Jin, H. Kim, M. H. Jo, C. Lee, J. Kim, S. Ryu, *ACS Nano* **2022**, *16*, 16385.

[19] J. Son, S. Son, P. Park, M. Kim, Z. Tao, J. Oh, T. Lee, S. Lee, J. Kim, K. Zhang, K. Cho, T. Kamiyama, J. H. Lee, K. F. Mak, J. Shan, M. Kim, J. G. Park, J. Lee, *ACS Nano* **2021**, *15*, 16904.

[20] F. Wu, M. Gibertini, K. Watanabe, T. Taniguchi, I. Gutiérrez-Lezama, N. Ubrig, A. F. Morpurgo, *Adv. Mater.* **2023**, 2211653.

[21] S. Qi, D. Chen, K. Chen, J. Liu, G. Chen, B. Luo, H. Cui, L. Jia, J. Li, M. Huang, Y. Song, S. Han, L. Tong, P. Yu, Y. Liu, H. Wu, S. Wu, J. Xiao, R. Shindou, X. C. Xie, J. H. Chen, *Nat. Commun.* **2023**, *14*, 1.

[22] M. Šiškins, S. Kurdi, M. Lee, B. J. Slotboom, W. Xing, S. Mañas-Valero, E. Coronado, S. Jia, W. Han, T. van der Sar, H. S. van der Zant, P. G. Steeneken, *npj 2D Mater. Appl.* **2022**, *6*, 1.

[23] M. J. A. Houmes, G. Baglioni, M. Šiškins, M. Lee, D. L. Esteras, A. M. Ruiz, S. Mañas-Valero, C. Boix-Constant, J. J. Baldové, E. Coronado, Y. M. Blanter, P. G. Steeneken, H. S. J. van der Zant, (preprint) Arxiv:2303.11234, v2, **2023**, https://arxiv.org/abs/2303.11234v2.

[24] M. Lee, M. Šiškins, S. Mañas-Valero, E. Coronado, P. G. Steeneken, H. S. van der Zant, *Appl. Phys. Lett.* **2021**, *118*, 193105.

[25] M. Šiškins, M. Lee, S. Mañas-Valero, E. Coronado, Y. M. Blanter, H. S. van der Zant, P. G. Steeneken, *Nat. Commun.* **2020**, *11*, 2698.

[26] J. López-Cabrelles, S. Mañas-Valero, I. J. Vitórica-Yrezábal, M. Šiškins, M. Lee, P. G. Steeneken, H. S. V. D. Zant, G. M. Espallargas, E. Coronado, *J. Am. Chem. Soc.* **2021**, *143*, 18502.

[27] D. Davidovikj, Ph.D. thesis, TU Delft, **2018**.

[28] B.-L. Li, B.-L. Li, M.-L. Guo, J.-F. Chen, J.-W. Fang, B.-Y. Fan, Q. Zhou, Y. Wang, Y. Wang, H.-Z. Song, H.-Z. Song, X.-B. Niu, X.-B. Niu, K. Y. Arutyunov, K. Y. Arutyunov, G.-C. Guo, G.-C. Guo, G.-W. Deng, *Opt. Lett.* **2023**, *48*, 2571.

[29] M. T. Dove, H. Fang, *Rep. Prog. Phys.* **2016**, *79*, 066503.

[30] A. L. Goodwin, M. Calleja, M. J. Conterio, M. T. Dove, J. S. Evans, D. A. Keen, L. Peters, M. G. Tucker, *Science* **2008**, *319*, 794.

[31] D. Das, T. Jacobs, L. J. Barbour, *Nat. Mater.* **2010**, *9*, 36.

[32] Y. Peng, Z. Lin, G. Tian, J. Yang, P. Zhang, F. Wang, P. Gu, X. Liu, C.-W. Wang, M. Avdeev, F. Liu, D. Zhou, R. Han, P. Shen, W. Yang, S. Liu, Y. Ye, J. Yang, *Adv. Funct. Mater.* **2022**, *32*, 2106592.

[33] M. Joe, J. Lee, C. Lee, *Comput. Mater. Sci.* **2019**, *162*, 277.

[34] M. Joe, H. Lee, M. M. Alyörük, J. Lee, S. Y. Kim, C. Lee, J. H. Lee, *J. Condens. Matter Phys.* **2017**, *29*, 405801.

[35] P. Villars, springerMaterials (online database), Springer, Heidelberg (ed.) SpringerMaterials, https://materials.springer.com/isp/crystallographic/docs/sd_1000213.

[36] K. G. Lyon, G. L. Salinger, C. A. Swenson, G. K. White, *J. Appl. Phys.* **1997**, *48*, 865.

[37] D. A. Wahab, M. Augustin, S. M. Valero, W. Kuang, S. Jenkins, E. Coronado, I. V. Grigorieva, I. J. Vera-Marun, E. Navarro-Moratalla, R. F. L. Evans, K. S. Novoselov, E. J. G. Santos, *Adv. Mater.* **2020**, *33*, 2004138.

[38] P. J. Zomer, M. H. D. Guimarães, J. C. Brant, N. Tombros, B. J. van Wees, *Appl. Phys. Lett.* **2014**, *105*, 013101.